Journal of
www. biophotonics-journal.org
BIOPHOTONICS

WILEY-VCH

J. Biophotonics **5**, No. 5–6, 437–448 (2012) / **DOI** 10.1002/jbio.201200003

Journal of BIOPHOTONICS

FULL ARTICLE

Integrated multimodal optical microscopy for structural and functional imaging of engineered and natural skin

Youbo Zhao[1], *Benedikt W. Graf*[1,2], *Eric J. Chaney*[1], *Ziad Mahmassani*[3], *Eleni Antoniadou*[4], *Ross DeVolder*[5], *Hyunjoon Kong*[5], *Marni D. Boppart*[3], *and Stephen A. Boppart*[*,1,2,4,6]

[1] Biophotonics Imaging Laboratory, Beckman Institute for Advanced Science and Technology, University of Illinois at Urbana-Champaign, Urbana, IL 61801, USA
[2] Department of Electrical and Computer Engineering, University of Illinois at Urbana-Champaign, Urbana, IL 61801, USA
[3] Department of Kinesiology and Community Health, University of Illinois at Urbana-Champaign, Urbana, IL 61801, USA
[4] Department of Bioengineering, University of Illinois at Urbana-Champaign, Urbana, IL 61801, USA
[5] Department of Chemical and Biomolecular Engineering, University of Illinois at Urbana-Champaign, Urbana, IL 61801, USA
[6] Department of Internal Medicine, University of Illinois at Urbana-Champaign, Urbana, IL 61801, USA

Received 4 January 2012, revised 7 February 2012, accepted 7 February 2012
Published online 28 February 2012

Key words: skin, tissue engineering, microscopy, functional imaging, multiphoton fluorescence microscopy, fluorescence lifetime imaging microscopy, optical coherence tomography

An integrated multimodal optical microscope is demonstrated for high-resolution, structural and functional imaging of engineered and natural skin. This microscope incorporates multiple imaging modalities including optical coherence (OCM), multi-photon (MPM), and fluorescence lifetime imaging microscopy (FLIM), enabling simultaneous visualization of multiple contrast sources and mechanisms from cells and tissues. Spatially co-registered OCM/MPM/FLIM images of multi-layered skin tissues are obtained, which are formed based on complementary information provided by different modalities, i.e., scattering information from OCM, molecular information from MPM, and functional cellular metabolism states from FLIM. Cellular structures in both the dermis and epidermis, especially different morphological and physiological states of keratinocytes from different epidermal layers, are revealed by mutually-validating images. *In vivo* imaging of human skin is also investigated, which demonstrates the potential of multimodal microscopy for *in vivo* investigation during engineered skin engraftment. This integrated imaging technique and microscope show the potential for investigating cellular dynamics in developing engineered skin and following *in vivo* grafting, which will help refine the control and culturing conditions necessary to obtain more robust and physiologically-relevant engineered skin substitutes.

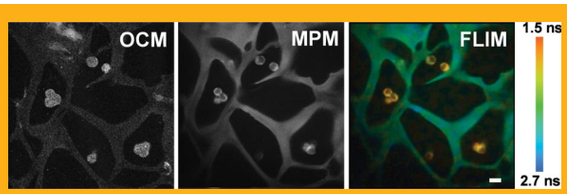

Multimodal microscopy images of a microporous 3D hydrogel scaffold seeded with 3T3 fibroblasts. Representative spatially co-registered images were generated based on different methodologies including optical coherence (OCM), multiphoton (MPM), and fluorescence lifetime imaging (FLIM) microscopy.

* Corresponding author: e-mail: boppart@illinois.edu, Phone: +1 217 244 7479, Fax: +1 217 333 5833

Journal of
BIOPHOTONICS

1. Introduction

Engineered skin equivalents have become important biomaterials for both basic research and clinical practice [1, 2]. Research-based applications of synthesized skin tissues, as an alternative to animal testing, have included tests of efficacy of pharmaceutical and cosmetic products [3], studies of toxicities of chemical agents [4], understanding of normal skin function (e.g. UV protection [5], wound healing) and dermatological disease pathogenesis [6]. Clinically, engraftment of engineered skin has emerged as a promising option for the treatment of skin loss, especially in the case of large-area injury or loss when autologous transplant sources are not sufficient [7, 8]. For all these applications, skin equivalents that have well-developed three-dimensional (3D) structures and mimic as many of the physiological and mechanical functions of native skin as possible, are always preferred.

Tissue engineering of skin is a delicate multistep procedure involving complex cell dynamics which interplay with culturing conditions and culturing materials [9]. The use of 3D topographic scaffold structures at the dermal-epidermal junction and the application of mechanical stimuli [10, 11] applied to developing tissues have been found to be important factors influencing the viability and functionality of engineered skin tissues. It has been shown that a capable multi-functional imaging instrument would greatly facilitate not only the investigation of developing engineered skin tissues, but also the clinical evaluation of successful *in vivo* engraftment, and thus help to evaluate and optimize the necessary culturing conditions to improve the applicability and outcome of engineered skin tissues in the treatment of skin injury, loss, and disease [12, 13].

Skin, including engineered skin constructs, is a spatially heterogeneous tissue with large variations in cellular composition and organization, both in states of health and disease. An advantageous imaging tool for skin is one that has sufficient resolution and contrast to directly observe both the structural and physiological or functional properties at different skin depths. Histology, the "gold standard", has been well-suited for the purpose of assessing cell morphology and organization, and other architectural aspects such as epidermal and dermal thickness, and orientation of collagen. However, histology procedures are destructive, and always the endpoint for the tissue under examination, making histology inappropriate for the evaluation of the real-time cellular dynamics and physiological functions of the skin. Ultrasound is non-invasive, but poorly suited for imaging skin because of its low resolution, typically on the order of 100 μm. High-frequency ultrasound imaging can achieve higher imaging resolution, such as less than 10 μm at 100 MHz frequency [14, 15], but is not commonly used for skin imaging, and requires contact and the use of an impedance-matching gel.

Optical coherence tomography (OCT) [16, 17] is an emerging biomedical imaging technology that has unique features, such as non-contact, non-invasive detection, higher resolution than ultrasound, better imaging depth than conventional confocal microscopy, and has been widely employed in the field of tissue engineering [11, 18, 19]. The limitations of OCT, however, include the relatively low resolution compared to histology, and deficient endogenous contrast when used without contrast agents. Nonlinear optical microscopy technologies, such as two-photon excitation fluorescence (TPEF) [20], second harmonic generation (SHG) [21], and coherent anti-Stokes Raman scattering (CARS) [22], provide subcellular resolution and unique contrast capabilities. These advanced microscopy techniques have drawn considerable attention from dermatologists [13, 23]. However, these microscopy techniques are plagued by shallow imaging depths and somewhat specific or limited contrast generation.

Given the different strengths and weaknesses associated with these different technologies or modalities, a great deal of research effort has been invested in the development of integrated microscopes that combine multiple modalities and enable co-registered images to leverage the advantages from multiple structural and functional contrast mechanisms. Multimodal microscopes such as an integrated multiphoton (MPM, including TPEF and SHG)/OCT [24], CARS/OCT [25], CARS/MPM [26], reflective confocal/TPEF/SHG [27, 28], fluorescence lifetime imaging microscopy (FLIM)/SHG/TPEF [29, 30] among others, have been demonstrated successfully for simultaneously visualizing multiple properties of the sample or specimen. In particular, the combination of optical coherence microscopy (OCM, the high-resolution variant of OCT [31]) and MPM has drawn considerable attention because this combination can provide co-registered structural and molecular information of the sample and possibly be based on a single laser source [32, 33]. Other than this combination, an integrated OCT and FLIM system has been demonstrated for simultaneous characterization of morphological and biochemical properties of tissue [34].

Fluorescence lifetime imaging microscopy is an established imaging methodology which is used to probe molecular level variations associated with biological activities, based on the changes in fluorescence lifetime of specific fluorophores [30, 35, 36]. It has been shown to be capable of monitoring protein-protein interactions [37], detecting environmental changes in biological systems (such as pH value, ion concentration, etc.), detecting early changes associated with certain cancers [38], and differentiating apoptosis and necrosis pathways [39, 40]. In particular, FLIM is a non-invasive method for monitoring

metabolic states of living cells, based on the lifetime variation of autofluorescence from reduced nicotinamide adenine dinucleotide (NADH) [39, 41]. A combination of FLIM with OCT has the potential clinical application for early detection of pathological changes in biological tissues. Unfortunately, because the two modalities have different working principles, the information provided by the two modalities is not completely spatially co-registered, i.e., 3D volumetric OCT morphology versus two-dimensional superficial maps of autofluorescence lifetime.

Here we report an integrated imaging platform which incorporates MPM, OCM, and FLIM, continuing our previous efforts for developing multimodal microscopy techniques [32, 42]. The combination of FLIM not only adds a new contrast capability to our previously developed OCM/MPM microscope, but more importantly enables one to monitor the metabolic activities of living tissue. This new multimodal-enabled integrated microscope is used to characterize multiple properties of tissue, based on an increasingly comprehensive set of information, i.e., scattering information from OCM, molecular information from MPM, and cellular metabolism from FLIM.

In this paper, real-time imaging of engineered and natural skin is demonstrated with this multimodal microscope. For well-developed bi-layer (dermis and epidermis) engineered skin tissues, detailed morphology of cells and structures from different layers were readily visualized with OCM and MPM, including keratinocytes in the epidermis, and fibroblasts and collagen in the dermis. Changes in morphology and the metabolic state of keratinocytes from different epidermal layers, which represents the complex, multi-step cornification process of keratinocytes, were observed with OCM and FLIM. The keratinization process was also manifested by time-lapse imaging with OCM and MPM. Complementary contrast capabilities were investigated by imaging fibroblasts seeded in 3D structured hydrogel scaffolds. *In vivo* imaging of human skin was also investigated, which explores the capability of this system for tracking the skin biology following engraftment of engineered skin tissue. Collectively, the use of a multimodal microscopy techniques in a single integrated imaging platform has the potential to improve our understanding and diagnostic capabilities in dermatology, and the development of engineered skin for tissue replacement.

2. Experiments and methods

In brief, the integrated OCM/MPM/FLIM imaging system is based on a single laser source, and a shared microscope frame, but with separated excitation beams and detection channels for different modalities. In our previous work on the development of an integrated OCM/MPM microscope, several unique strategies were implemented for seamless integration of different modalities. These strategies include a single laser source based on a dual-band arrangement, independently controlled excitation beams, and computational algorithms for correction of coherence curvature, for dispersion balance and correction, and for fast signal and image processing. With these techniques, we are able to optimize the performance of multiple imaging modalities simultaneously without compromising the advantages of the individual modes. Most of the methodologies presented here are inherited from our previous work, and detailed information can be found elsewhere [32, 43, 44].

The schematic of the integrated OCM/MPM/FLIM microscope is shown in Figure 1. For its optical source, a high-power, widely-tunable titanium:-sapphire laser (Mai-Tai HP, Spectra-Physics) is used,

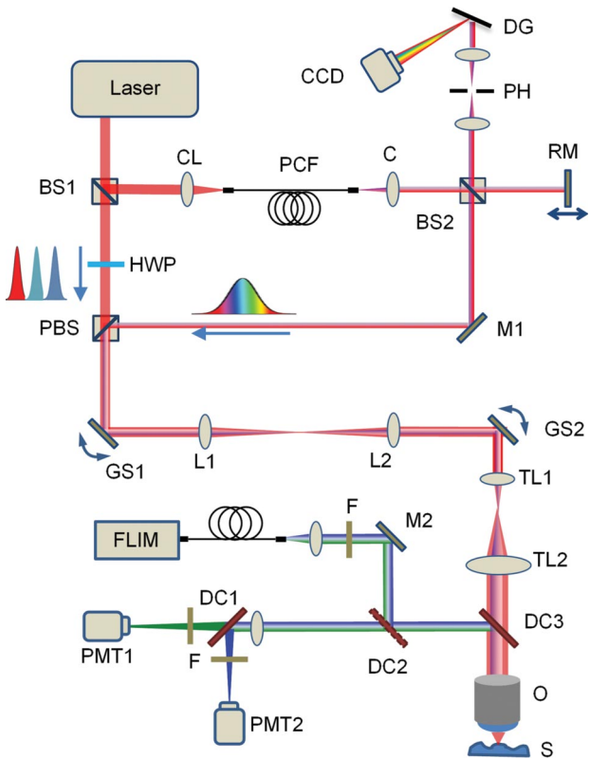

Figure 1 (online color at: www.biophotonics-journal.org) Schematic of the integrated optical microscope. Abbreviations: BS, beam splitter; C, collimator; CCD, charge-coupled device line-scan camera; CL, coupling lens; DC, dichroic mirror; DG, diffraction grating; F, filter; GS, galvanometer scanner; HWP, half-wave plate; L, lens; O, objective; M, high reflection mirror; PCF, photonic crystal fiber; PBS, polarizing beam splitter; PH, pinhole; PMT, photo-multiplier tube; RM, reference mirror; S, sample, TL, telescope lens.

Journal of
BIOPHOTONICS

which outputs 100 fs pulses at an 80 MHz repetition rate with a bandwidth of 10 nm at a tunable center wavelength within the range of 730–1000 nm. The linearly-polarized output (with maximum average power of 3 W) from this laser is divided by a 90/10 beam-splitter into two portions. The 10% portion, with narrowband but wide wavelength tuning range, is used for excitation of MPM and FLIM. The higher power beam is coupled into a photonic crystal fiber (LMA-PM-5, NKT Photonics) where through self-phase modulation, the spectrum is broadened to 100–150 nm FWHM, depending on the center wavelength of the laser. The light from the fiber, which serves as the OCM source, is collimated with an objective and then directed to the OCM interferometer. The polarization-maintaining fiber ensures that the OCM beam remains linearly polarized. The OCM sample arm and the MPM/FLIM beams are combined by a polarizing beam splitter, with polarization of the MPM/FLIM being controlled by a half wave plate. The power of the MPM and OCM sources is independently controlled by a set of neutral density filters.

The collinearly-propagating OCM sample arm and MPM beams are expanded by a telescope and focused by a microscope objective (XLUMP20X, 0.95 NA, water immersion, Olympus) into the sample. While the back aperture of the objective is fully filled by the MPM beam to obtain an optimal resolution, the beam diameter of the OCM sample arm beam is controlled by using a different collimator or putting a telescope right after the collimator. By doing this, we are able to control the effective NA of the OCM beam to obtain an optimal balance between resolution and depth-of-field. For all the OCM images in this paper, if not specifically mentioned, we used effective NA of 0.65. The sample is positioned on a motorized stage which can translate the sample in three directions. A pair of galvanometers (Micromax 671, Cambridge Technology) positioned before the telescope is used to scan the beam across the sample. The spectral interference pattern of the reference and sample arm beams is detected for OCM acquisition by a spectrometer which is based on a diffraction grating and CCD line camera (Piranha2 2k, Dalsa). The frame rate for the line camera depends on the speed and mode of image acquisition (galvanometer), and can be up to 32 kHz. OCM images are generated after several processing steps including compensating for unbalanced dispersion in the sample arm, compensating for non-uniform distribution of the spectrum on the CCD due to nonlinearity of the diffraction grating, and correction for the coherence curvature due to the mismatch between the coherence gate and the confocal gate across the field-of-view [32].

For MPM and FLIM, the epi-collected signals are diverted by a long-pass dichroic mirror and band-pass filtered. The dichroic mirror can be flipped to opposite directions to steer the fluorescence signals for either MPM or FLIM. For MPM, the signal is either divided by the dichroic mirrors or filtered into different channels for parallel detection of various fluorescence or SHG signals. The fluorescence signals are detected by photomultiplier tubes (H7421, Hamamatsu). For FLIM, the fluorescence signals are collected by a multimode fiber and then coupled into a grating-based polychromator and detected by a 16-channel PMT. The output pulses of the PMT channels are digitized and analyzed by a time-correlated single-photon counting board (SPC 150, Becker & Hickle). FLIM analyses are performed by commercial software (SPCimage, Becker & Hickle). All the FLIM images in this paper, if not specifically mentioned, were obtained by first integrating all 16 channels and then fitting the appropriate lifetime decay.

Full thickness bi-layer engineered skin tissues (EpiDerm FT400, MatTek Corp.) were used to demonstrate the performance of this integrated microscope. The engineered skin consists of normal, human-derived epidermal keratinocytes, and normal, human-derived dermal fibroblasts, which form a multi-layered, highly differentiated model of the human dermis and epidermis. The epidermis consists of mostly keratinocytes of different physiological states and the dermal compartment is composed of a collagen matrix containing viable human fibroblasts. The complicated multi-layered structure and physiologically-rich cellular state make this engineered skin an excellent sample to test the imaging and diagnostic capabilities of our system. The tissues were cultured in an incubator with 5% CO_2 at 37 °C, and nourished daily with 2.5 ml Dulbecco's Modified Eagle's Medium (pH 7.4). The tissues were maintained in single well tissue culture plate inserts (Costar Snapwell™, Corning) and at an air-liquid interface. During imaging, the engineered tissues were kept in a Petri dish with fresh culturing media at room temperature. The Petri dish was slightly modified with embedded stainless steel pins to hold the tissues and limit movement during imaging. The Petri dish was also covered by a specially designed insert with an optical window to help maintain the sterile culture environment of the tissue during imaging. After each imaging session, which required less than two hours, the tissues were returned back to their original culturing conditions in a commercial incubator.

Fibroblasts seeded in microporous hydrogel scaffolds were also used in these experiments, and were prepared as follows. Alginate (LF20/40, FMC BioPolymer, Rockland, ME), weight-average molecule weight (MW) ~250,000 g mol^{-1}, was dissolved in a 0.1 M MES (2-(N-morpholino)ethanesulfonic acid) buffer (pH 6.4, Sigma-Aldrich, St. Louis, MO). The 2% (w/w) sodium alginate solution was filtered and 1-hydroxybenzotriazole (HOBt, Fluka, St. Louis,

MO), 1-ethyl-3-(3-dimethylaminopropyl) carbodiimide (EDC, Thermo Scientific, Hanover Park, IL), and adipic acid dihydrazide (AAD), Sigma-Aldrich) were dissolved in the alginate solution, and the pH was adjusted to 6.0. The molar ratio of EDC : HOBt : AAD was 1.0 : 0.5 : 0.2. Subsequently, gel sheets were made on glass slides and hydrogel disks with diameters of 5 mm were punched out and incubated in phosphate-buffered saline, at pH 7.4 (PBS) and at 37 °C for 6 hr before characterization. The water content of the initial cross-linked hydrogel was 97 wt%, which was determined by measuring the hydrogel weight before and after swelling at 37 °C in millipore water (Nanopure Diamond^{TM}, Barnstead). The disks were then frozen at −20 °C for 6 hr and lyophilized at −60 °C. Finally, the gel discs were irradiated with UV light ($\lambda_{max} = 254$ nm, Jelight Co. Model 20, Irvine, CA) for 2 hr for sterilization purposes. NIH 3T3 fibroblasts labeled with CellLight Reagents (Life Technologies) were suspended in the pre-gel solution at a density of 1×10^6 cells ml^{-1}. Cell viability was checked with MTT assay analysis at different time points within a few days of cell seeding.

Dorsal hand skin of a human volunteer served as the natural skin specimen for *in vivo* imaging experiments. An imaging mount, which consisted of a thin glass coverslip mounted to a rigid holder, was designed to keep the skin stabilized during image acquisition. A small amount of glycerol was applied to the skin prior to imaging to serve as an index matching agent. All imaging was done in accordance with a protocol approved by the Institutional Review Board at the University of Illinois at Urbana-Champaign.

3. Results

Depth-resolved OCM/MPM images of a full thickness engineered skin sample are shown in Figure 2. All images, composed of 256 × 256 pixels, were obtained at a rate of about 3 seconds per frame. All the OCM and MPM images in this paper, if not specifically mentioned, were generated with the same parameters, and without any image averaging or processing. All the images at different depths (from all three modalities) were obtained by axially translating the samples via the three-axis translation stage with the incidence laser power left unchanged. The OCM images were generated based on the backscattered light from the tissue, and the OCM depth resolution was determined by the coherence gate based on the same principle as in OCT. In our case, the depth resolution was estimated to be 1.5 μm, which was determined by the 150 nm bandwidth of the supercontinuum-generated OCM beam from the photonic crystal fiber. The signals in the MPM images are primarily two-photon excited autofluorescence of NADH from cells and second harmonic generation from collagen. The axial and transverse resolutions for MPM were experimentally determined by imaging fluorescent beads and were measured to be 0.8 μm and 0.5 μm, respectively. While acquiring the MPM images, a short-pass filter was used, and the autofluorescence and SHG signals were not separated. The input laser energies for OCM and MPM were 5 and 22 mW, respectively. The center wavelengths used for OCM and MPM were 800 nm and 760 nm, respectively. A histology image is shown in Figure 2(b) for comparison. The co-registration of images from the two different modalities is shown by the merged image in Figure 2(c).

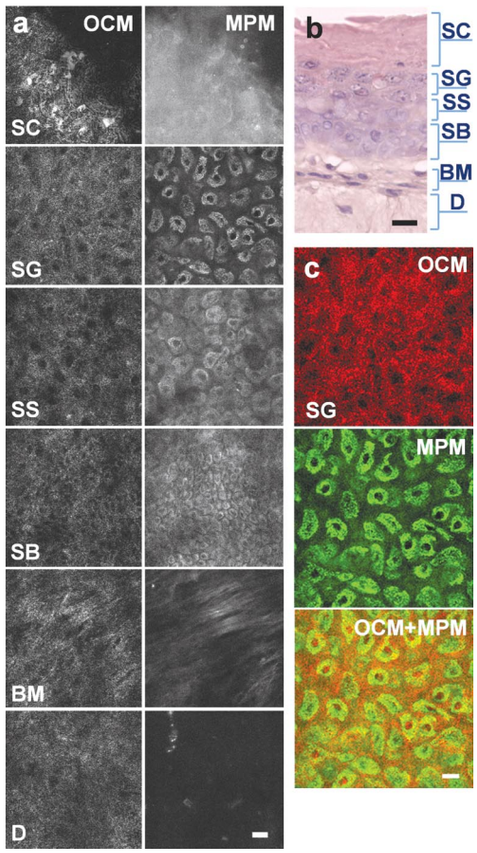

Figure 2 (online color at: www.biophotonics-journal.org) OCM and MPM images from a bi-layer engineered skin sample. (**a**) OCM (left column) and MPM (right column) images from different layers of the engineered skin tissue. (**b**) Hematoxylin and eosin stained histology image of the tissue. (**c**) Pseudo-color images of OCM (top), MPM (middle) and merged OCM and MPM (bottom). Abbreviations: SC, stratum corneum; SG, stratum granulosum; SS, stratum spinosum; SB, stratum basale; BM, basal membrane; D, dermis. Scale bars represent 20 μm.

Journal of
BIOPHOTONICS

As shown by the OCM and MPM images in Figure 2, different cellular architecture at different depths is visualized, including different morphologies of keratinocytes from different layers, i.e., stratum corneum (SC, stratified keratinocytes), stratum granulosum (SG), stratum spinosum (SS), stratum basale (SB), as well as collagen and fibroblasts in the dermis. Based on the different physics for contrast and image formation, the two modalities provide different but complementary information of the sample. In particular, the morphological changes of the keratinocytes progressing from the inner layers to the outer layers reflect the evolution of the physiological state at different points along the complicated process of keratinization. It is also worthwhile to note that the SHG signals from the collagen are also vitally important information about the health and integrity of skin [45], and have been used to investigate dermal diseases *in vivo* that are associated with changes in collagen and elastin such as scleroderma or graft versus host disease [13].

As a potentially non-invasive imaging method, another advantage of this integrated microscopy is for the real-time monitoring of the dynamics or development of living tissue over time. OCM and MPM images from different days of the engineered skin tissue under normal culturing conditions are shown in Figure 3. Comparison between the OCM and MPM images on different days further demonstrates the usefulness of the complementary information gained from the two modalities. It is seen from the time-lapse image sequence that more keratinocytes have migrated from deeper layers to more superficial layers, and are losing nuclei and organelles over time, which actually is one way to validate the process of keratinization. The process is further validated by the comparison of histology results, which shows that the stratum corneum is thicker after a few days. As shown by the images, the MPM images provide better visualization of the cellular structures during the early days, while the OCM images provide better observation of the keratinized cells during the later days of culture, where cells are losing their normal morphology and organelles.

Another important advantage of the multimodal microscope described here is the integration of FLIM with the other two modalities, which extends the functional imaging capabilities of the system. Figure 4 shows OCM and FLIM images of keratinocytes at different epidermal layers. The FLIM images are composed of 256 $\times$ 256 pixels and were generated in about 4 minutes. The lifetimes were analysed based on a simulation model composed of two exponential components, which correspond to the free and enzyme-bound NADH. The model is expressed by $I(t) = a_1\, \mathrm{e}^{-t/\tau_1} + a_2\, \mathrm{e}^{-t/\tau_2}$, where a_1, τ_2, and a_2, τ_2 are the amplitudes and lifetimes of free and bound

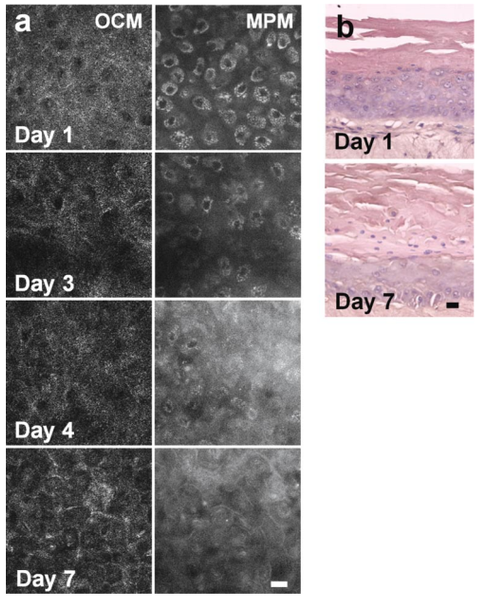

Figure 3 (online color at: www.biophotonics-journal.org) Time-lapse OCM and MPM images from an engineered skin sample. (**a**) OCM (left column) and MPM (right column) images from the stratum spinosum layers of the engineered skin after increasing days of culture. (**b**) Comparison of hematoxylin and eosin stained histology images of the engineered skin tissue on Day 1 (upper) and Day 7 (lower) of culture. Scale bars represent 20 μm.

NADH, respectively. The average lifetime is given by $\tau_{\mathrm{ave}} = (a_1\tau_1 + a_2\tau_2)/(a_1 + a_2)$. It has been demonstrated that both the average lifetime and the ratio (a_1/a_2) of amplitudes of the two components can be used to probe the metabolic activities of cells [39, 41]. In this case, longer average lifetime or a smaller ratio corresponds to a higher level of metabolic activity. The average lifetime or ratio shown in Figure 4 was obtained by analysing the decay rate of the integrated fluorescence over the entire detection spectrum of the FLIM system, which ranges from 374 to 565 nm. Shown by the lifetime images and the corresponding histograms in Figure 4, the average lifetime is getting longer and the ratio of the two components is getting lower, from the inner basal layer to the spinous layer. These results are in good agreement with the difference in metabolic level of keratinocytes from different epidermal layers, i.e., the lower metabolic states in the inner (basal) layers and higher metabolic states in the outer (spinous) layers.

It should be noted that the decay dynamic of autofluorescence from a mixture of free and protein bound NADH is a complex multi-exponential process, which may need a more complicated model and data processing method to analyze [46]. Here it is approximated using the frequently used approxima-

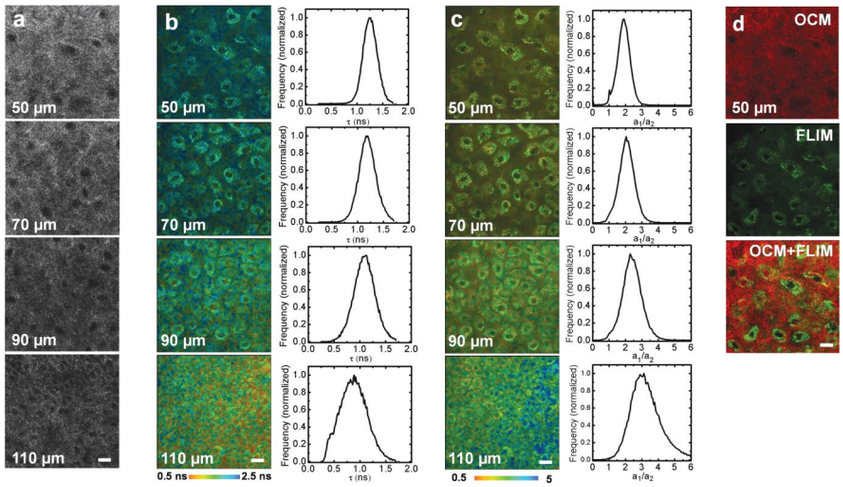

Figure 4 (online color at: www.biophotonics-journal.org) OCM and FLIM images from an engineered skin tissue. (**a**) OCM images from different depths (zero microns is at the surface) in the engineered skin tissue. (**b**) FLIM images and corresponding histograms of average lifetime at different depths of the skin tissue. (**c**) FLIM images and corresponding histograms of free-to-bound amplitude ratio at different depths of the skin tissue. (**d**) Pseudo-color images of OCM (top), FLIM (middle) and merged OCM and FLIM (bottom). Scale bars represent 20 µm.

tion of a bi-exponential decay model. In addition to the level of the metabolism, the change in average lifetime and/or ratio of the two exponential components is also an indicator of shifts between glycolytic and oxidative metabolism, which has been used for the detection of a tumor margin [38]. This change could also reflect the shorter lifetime (lower metabolism) of the basal layer within the engineered skin, compared to the *in vivo* skin, which could be attributed to the lower oxygen concentration within the basal layer of the engineered skin.

Incorporation of FLIM also adds new functional contrast capabilities to the imaging platform, which is demonstrated in Figure 5, showing images of a microporous fibroblast-seeded hydrogel scaffold that were obtained with different modalities. A center wavelength of 760 nm was used for both modalities, and the incident laser power was 5 and 17 mW for OCM and FLIM, respectively. It is also shown in Figure 5 that the cell morphology and the microporous structure of the hydrogel are clearly differentiated and well-observed with both OCM and MPM, in comparison to the phase contrast image. Because of the spectral overlap between the autofluorescence from the hydrogel and the autofluorescence from cells, which is illustrated by spectroscopic analysis (Figure 5(b)), they are not well separated in the MPM image, which was generated based on the spectrally-integrated signals. In contrast, FLIM clearly distinguishes them based on the different lifetimes of the two fluorescence emissions, showing different colors for the hydrogel and the cells. In this case, the lifetime was obtained by fitting the decay measurements with a single exponential model. The spectra in Figure 5(b) were retrieved from the FLIM data which was measured based on a 16-channel monochromator.

OCM/FLIM images from different depths of *in vivo* human skin are shown in Figure 6. The images were obtained from a dorsal hand of a human volunteer. The laser power used was 5 and 17 mW for OCM and FLIM, respectively, and the center wave-

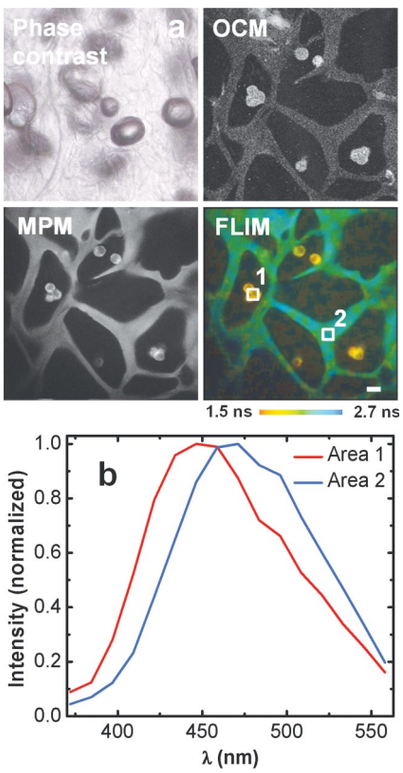

Figure 5 (online color at: www.biophotonics-journal.org) Multimodal images of a microporous 3D hydrogel scaffold seeded with 3T3 fibroblasts. (**a**) Representative images based on phase contrast, OCM, MPM, and FLIM. (**b**) Integrated spectra from two different areas in the FLIM image showing spectral overlap, but which can still be distinctly differentiated based on lifetimes. Scale bar represents 20 µm.

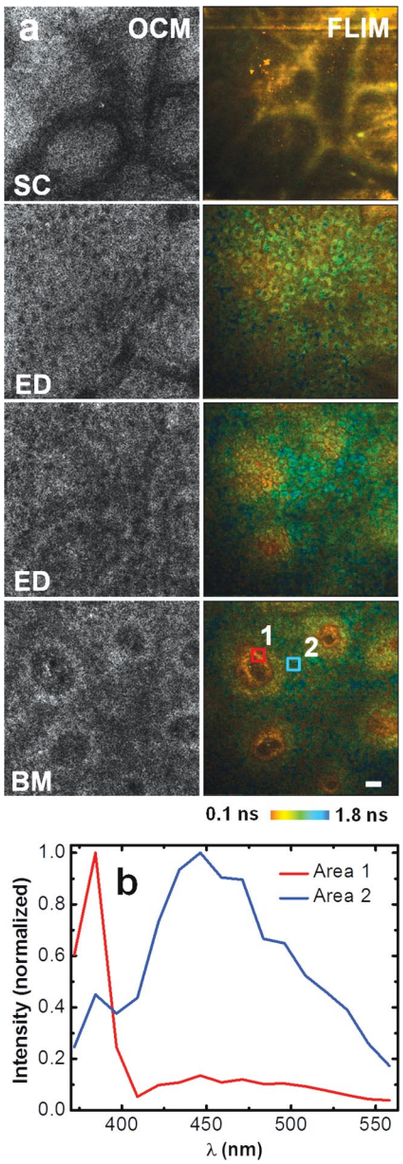

Figure 6 (online color at: www.biophotonics-journal.org) OCM and FLIM images of *in vivo* human skin. (**a**) OCM (left column) and FLIM (right colum) images. (**b**) Integrated FLIM spectra of two different areas noted in the FLIM image from the basal membrane layer. Abbreviations: SC, stratum corneum; ED, epidermis; SB, stratum basale; BM, basal membrane; D, dermis. Scale bar represents 20 μm.

length was 760 nm for both the two modalities. Each FLIM image of *in vivo* skin was acquired in 30 s. FLIM images show the spatial distribution of average lifetime which is based on the same procedures for generation of images in Figure 4(b). *In vivo* skin structures at different depths, including the topography of the stratum corneum, the cellular morphology of keratinocytes in the superficial epidermis, and the dermal papillae projections of the basal membrane can all be visualized in both OCM and FLIM images, as shown in Figure 6. Lifetime changes (indicated by different colors) likely indicate alterations in metabolic states and/or contributions from different chromophores. For example, the spectral analysis in Figure 6(b) shows strong SHG signal from the areas surrounding the papillae projections and broadband autofluorescence from the cellular structures. The fluorescence lifetime of *in vivo* skin is somewhat different from that of engineered skin. Specifically, the lifetime from the basal layer in *in vivo* skin is longer than from the basal layer in the engineered skin, which could be due to the difference in nutrient supply between *in vivo* natural skin and *in vitro* engineered skin. The measured lifetime from *in vivo* human skin in our study is in good agreement with those *in vivo* FLIM results reported by other researchers [30, 36]. Further correlations between the measured data and the physiological changes in the skin are needed, as well as more comprehensive and systematic imaging investigations [36].

4. Discussion

As shown by the above results, the use of an integrated multimodal microscope offers the capability to visualize the complicated multilayer architecture of both *in vitro* engineered human skin and natural *in vivo* human skin. The main structures of engineered skin, including fibroblasts and collagen in the dermis, and different morphologies and physiological states of keratinocytes in the epidermis, are visualized by depth-resolved images. Surface topography, cellular morphology, and 3D projections of dermal papillae are observed in *in vivo* human skin imaging. Complementary information obtained with this integrated microscope consists of the structural architecture, cellular morphology, and metabolic states, based on the corresponding OCM, MPM, and FLIM modalities. The spatially co-registered images from different modalities actually provide a matrix of vectors for each pixel, rather than the one dimensional scalar information provided by any single modality. We believe this matrix information will enable one to ultimately obtain a better understanding of the physiology of the localized tissue or cells.

Time-lapse images demonstrate the capability of this microscope and methodology for monitoring the developmental processes of skin in real time. These features enable one to investigate the development and cellular dynamics in engineered skin tissues, as well as facilitate our understanding of the function and physiology of natural *in vivo* human skin. For example, the first and most important protective bar-

rier of skin is guaranteed by the characteristic architecture of the stratum corneum. This uppermost layer of the epidermis consists of dead cells (corneocytes) that lack nuclei and organelles. Generation and renewal of the stratum corneum is ensured by the transformation of keratinocytes into corneocytes [47]. This process, which is the main feature of epidermal differentiation, starts with the proliferation of keratinocytes in the stratum basale and ends with the cornification of cells (technically dead). During this process, the keratinocytes migrate toward the surface through the epidermal layers, including the stratum basale, stratum spinosum, stratum granulosum, and the stratum corneum. The cells appear with different morphological and physiological states with each of these layers. As shown by the images in Figures 2 and 4, the morphological differences in these epidermal layers are readily revealed by OCM and MPM images, and the different metabolic states associated with these different physiological states are manifested in the FLIM images. Time-lapse images in Figure 3 also demonstrate the keratinization process over time.

While each modality has unique features for imaging the tissue, the complementary information provided by the spatially co-registered images provides additional insight into the tissue structure and function, and mutually validates the results obtained with the individual modalities. As shown by the OCM and MPM images in Figure 3, while MPM provides better visualization of the cellular structure, OCM shows advantages when cells are close to cornification and lose their cellular shape and organelles (and thus the spatially confined fluorophores on which MPM images are based). In practical imaging procedures, the different modalities also facilitate each other to obtain the desired imaging results. For example, because OCM is advantageous for imaging the overall structures present within the sample based on the scattering contrast, and it uses relatively lower incident laser power, OCM is always used as the guiding mode to locate the desired imaging area of interest. This is particularly important in the case of using the OCM and FLIM modes, given the relatively slow imaging speed of FLIM (usually several minutes for one image). The slow imaging speed of FLIM also necessitates the use of the fast MPM mode for locating desired regions of interest, although MPM images can also be generated based on the FLIM data. The complicated processes for signal detection in FLIM, including fiber collection of fluorescence signal, spectral separation by the monochromator, and time-resolved photon counting approaches, result in the low signal detection efficiency and thus the slow imaging speed for FLIM. Therefore, the MPM mode with much higher signal detection efficiency and imaging speed is more often the preferred way for generating MPM images.

OCM offers other potential capabilities for the investigation of engineered and natural skin. Compared to reflection mode confocal microscopy, which is another widely used microscopy technique that is able to generate 3D images based on the scattering properties of samples, OCM is advantageous in that its axial resolution is determined by the bandwidth of light source rather than the numerical aperture of the objective. This feature enables the OCM modality to be flexibly modified for a larger field-of-view and depth-of-field. In our system, this can be done be changing the beam diameter of the OCM beam at the back aperture of the objective to alter the effective NA of OCM while keeping the MPM parameters unaffected. Because OCM utilizes coherence gating in addition to the confocal gating utilized in confocal microscopy, OCM is able to image considerably deeper into high-scattering tissues, such as skin, because the added coherence gating rejects multiply-scattered photons that only contribute to background noise in confocal microscopy [48]. There are also many variants of OCT/OCM that allow complementary features of the sample to be observed. These variants include polarization-sensitive OCT for visualizing tissue birefringence due to the presence and orientation of collagen fibers [49, 50], optical coherence elastography that is capable of measuring biomechanical parameters of the sample [51–53], and magnetomotive OCT used to enhance imaging contrast [54]. These additive imaging modalities will be explored in the future to further characterize the structural morphology and the functional and molecular physiology of engineered and natural skin.

5. Conclusions

In conclusion, we have demonstrated a unique integrated OCM/MPM/FLIM microscope that is capable of multimodal characterization and evaluation of engineered and natural skin tissues. With the capability for *in vivo* imaging of human skin, this multimodal microscope also represents a potentially powerful tool for clinical dermatological studies, provided that remaining technical issues are addressed, such as a better design of a dark box or a miniaturized stray light-limiting enclosure surrounding the imaging site, and increased flexibility of the imaging probe with better optical arrangement. Combined with microscope-compatible bioreactors, which are under design development in our lab, this imaging platform will enable one to monitor the developmental processes of engineered skin tissue in culture, and the cellular and functional dynamics of skin tissues during processes such as repair and regeneration in wound healing. These results lay the foundation for

future work using this multimodal microscopy approach longitudinally over time to investigate and optimize the culturing of engineered skin tissues, to track cell and tissue changes under different biochemical and biomechanical culturing conditions, and to evaluate the *in vivo* host skin response during the engraftment of engineered skin used in the treatment for skin injury or loss.

Acknowledgements We thank Dr. Marina Marjanovic for her helpful discussions and assistance with this research, and Mr. Darold Spillman for his technical, logistical, and information-technology support to this research. This research was supported in part by grants from the National Science Foundation (CBET 08-52658 ARRA, CBET 10-33906, S.A.B.). Benedikt Graf was supported by the Pre-doctoral National Institutes of Health Environmental Health Sciences Training Program in Endocrine, Developmental and Reproductive Toxicology at the University of Illinois at Urbana-Champaign. Additional information can be found at http://biophotonics.illinois.edu.

Youbo Zhao received his B.S. degree in applied physics from Beijing Institute of Technology, Beijing, China, in 1997, and his Ph.D. degree in optical engineering from Nankai University, Tianjin, China, in 2007. He is currently a postdoctoral research associate in the Biophotonics Imaging Laboratory at the University of Illinois at Urbana-Champaign, Urbana, IL. His research interests include developing and using novel optical imaging technologies for biomedical studies.

Benedikt W. Graf is a Ph.D. candidate in electrical and computer engineering at the University of Illinois at Urbana-Champaign. He is a research assistant in the Biophotonics Imaging Laboratory at the Beckman Institute for Advanced Science and Technology. His research interests include the development of multimodal optical imaging techniques for *in vivo* imaging of skin for both clinical and research applications. Research applications include tracking of stem cells in live mouse skin during wound healing.

Eric J. Chaney received his B.S. degree in biology from the University of Evansville, Evansville, Indiana, in 1992. From 1993 to 1997, he worked as a research assistant at the Indiana University School of Medicine, Indiana State University, Terre Haute. From 1997 to 2000, he worked as a transmission electron microscope technician at the University of Illinois at Urbana-Champaign. Since 2000, he has been a research scientist in molecular biology at the Biophotonics Imaging Laboratory, Beckman Institute, University of Illinois, Urbana-Champaign.

Ziad Mahmassani received his B.S. degree in bioengineering from the University of Maryland, College Park, Maryland. He is now a graduate student in the Department of Kinesiology and Community Health at the University of Illinois at Urbana-Champaign. His research focuses on regulation of muscle stem cells by mechanical strain.

Eleni V. Antoniadou is a Ph.D. candidate in bioengineering at the University of Illinois at Urbana-Champaign, USA. She holds a M.S. degree in nanotechnology and regenerative medicine from the Medical School of the University College London. She is currently a research assistant in the Tissue Engineering, Biomaterials and Stem Cell Niche Lab of the Chemical and Biomolecular Engineering Department. Her research interests include regenerative medicine applications, the development of artificial organs, and tissue engineering.

Ross DeVolder received his B.S. degree in Chemical Engineering from the University of Iowa in 2008, and his M.S. in Chemical Engineering from the University of Illinois in 2010. He is currently a graduate student in the chemical engineering department at the University of Illinois, Urbana-Champaign, working in Dr. Hyunjoon Kong's research group. His research interests include designing polymeric based materials with controllable properties for a wide array of applications.

Hyunjoon Kong is an assistant professor in the Department of Chemical and Biomolecular Engineering. He also holds affiliations with the Department of Bioengineering, Center for Biophysics, and Computational Biology and Neuroscience Program. He received his engineering education from the University of Michigan (Ph.D. 2001), and performed post-doctoral research at the University of Michigan and Harvard University. He joined the University of Illinois in 2007. His current research is focused on the design of biomaterials used for tissue regeneration, drug delivery, and imaging.

Marni D. Boppart is an assistant professor in the College of Applied Health Sciences, University of Illinois at Urbana-Champaign (UIUC), and holds a full-time faculty appointment at the Beckman Institute. She received her B.S. in Cell Biology from the University of New Hampshire, her M.S. in Cell Biology from Creighton University, and her Sc.D. in Applied Anatomy and Physiology from Boston University. She completed postdoctoral training at Harvard University and UIUC in Cell and Developmental Biology. Her current research interests include cellular biomechanics and the role for mesenchymal stem cells in muscle.

Stephen A. Boppart is currently a Bliss Professor of Engineering in the Departments of Electrical and Computer Engineering, Bioengineering, and Medicine, University of Illinois at Urbana-Champaign. He received the B.S. degree in electrical and bioengineering and the M.S. degree in electrical engineering from the University of Illinois at Urbana-Champaign, Urbana, IL, in 1990 and 1991, respectively, the Ph.D. degree in electrical and medical engineering from the Massachusetts Institute of Technology, Cambridge, in 1998, and the M.D. degree from Harvard Medical School, Boston, MA, in 2000. His research interests include the development of novel optical imaging technologies for biological and medical applications, with particular emphasis on translating these to clinical applications.

References

[1] D. M. Supp and S. T. Boyce, Clin. Dermatol. **23**, 403–412 (2005).
[2] S. MacNeil, Nature **445**, 874–880 (2007).
[3] C. Asbill, N. Kim, A. El-Kattan, K. Creek, P. Wertz, and B. Michniak, Pharm. Res. **17**, 1092–1097 (2000).
[4] I. Canton, D. M. Cole, E. H. Kemp, P. F. Watson, J. Chunthapong, A. J. Ryan, S. MacNeil, and J. W. Haycock, Biotechnol. Bioeng. **106**, 794–803 (2010).
[5] N. Bechetoille, C. Dezutter-Dambuyant, O. Damour, V. Andre, I. Orly, and E. Perrier, Tissue Eng. **13**, 2667–2679 (2007).
[6] M. Cario-Andre, C. Pain, Y. Gauthier, V. Casoli, and A. Taieb, Pigment Cell Res. **19**, 434–442 (2006).
[7] S. C. Rizzi, Z. Upton, K. Bott, and T. R. Dargaville, Expert Rev. Med. Devices **7**, 143–154 (2010).
[8] Y. M. Bello and T. J. Phillips, JAMA **283**, 716–718 (2000).
[9] A. F. Black, C. Bouez, E. Perrier, K. Schlotmann, F. Chapuis, and O. Damour, Tissue Eng. **11**, 723–733 (2005).
[10] H. M. Powell, K. L. McFarland, D. L. Butler, D. M. Supp, and S. T. Boyce, Tissue Eng. Part A **16**, 1083–1092 (2010).
[11] W. Tan, C. Vinegoni, J. J. Norman, T. A. Desai, and S. A. Boppart, Microsc. Res. Tech. **70**, 361–371 (2007).
[12] G. Lammers, P. D. H. M. Verhaegen, M. M. W. Ulrich, J. Schalkwijk, E. Middelkoop, D. Weiland, S. T. M. Nillesen, T. H. Van Kuppevelt, and W. F. Daamen, Tissue Eng. Part B-Rev. **17**, 33–55 (2011).
[13] K. M. Hanson and C. J. Bardeen, Photochem. Photobiol. **85**, 33–44 (2009).
[14] S. El Gammal, C. El Gammal, K. Kaspar, C. Pieck, P. Altmeyer, M. Vogt, and H. Ermert, J. Invest. Dermatol. **113**, 821–829 (1999).
[15] C. Passmann and H. Ermert, IEEE T. Ultrason. Ferr. **43**, 545–552 (1996).
[16] S. A. Boppart, B. E. Bouma, C. Pitris, J. F. Southern, M. E. Brezinski, and J. G. Fujimoto, Nat. Med. **4**, 861–865 (1998).
[17] D. Huang, E. Swanson, C. Lin, J. Schuman, W. Stinson, W. Chang, M. Hee, T. Flotte, K. Gregory, C. Puliafito, and J. G. Fujimoto, Science **254**, 1178–1181 (1991).
[18] X. Liang, B. W. Graf, and S. A. Boppart, J. Biophotonics **2**, 643–55 (2009).
[19] W. Tan, A. L. Oldenburg, J. J. Norman, T. A. Desai, and S. A. Boppart, Opt. Express **14**, 7159–7171 (2006).
[20] W. Denk, J. Strickler, and W. Webb, Science **248**, 73–76 (1990).
[21] P. J. Campagnola and L. M. Loew, Nat. Biotechnol. **21**, 1356–1360 (2003).
[22] J. X. Cheng, Y. K. Jia, G. F. Zheng, and X. S. Xie, Biophys. J. **83**, 502–509 (2002).
[23] L. H. Laiho, S. Pelet, T. M. Hancewicz, P. D. Kaplan, and P. T. C. So, J. Biomed. Opt. **10**, 024016 (2005).
[24] B. Jeong, B. Lee, M. S. Jang, H. Nam, S. J. Yoon, T. Wang, J. Doh, B.-G. Yang, M. H. Jang, and K. H. Kim, Opt. Express **19**, 13089–13096 (2011).
[25] C. Hoffmann, B. Hofer, A. Unterhuber, B. Poavzay, U. Morgner, and W. Drexler, Proc. SPIE **7892**, 78920B (2011).
[26] C. S. Y. Wong, I. Robinson, M. A. Ochsenkühn, J. Arlt, W. J. Hossack, and J. Crain, Biomed. Opt. Express **2**, 2504–2516 (2011).
[27] S. H. Choi, W. H. Kim, Y. J. Lee, H. Lee, W. J. Lee, J. D. Yang, J. W. Shim, and J. W. Kim, J. Opt. Soc. Korea **15**, 61–67 (2011).
[28] B. R. Masters and P. T. C. So, Opt. Express **8**, 2–10 (2001).
[29] A. Zoumi, A. Yeh, and B. J. Tromberg, P. Natl. Acad. Sci. U.S.A. **99**, 11014–11019 (2002).
[30] E. Benati, V. Bellini, S. Borsari, C. Dunsby, C. Ferrari, P. French, M. Guanti, D. Guardoli, K. Koenig, G. Pellacani, G. Ponti, S. Schianchi, C. Talbot, and S. Seidenari, Skin Res. Technol. **17**, 295–303 (2011).
[31] A. D. Aguirre, P. Hsiung, T. H. Ko, I. Hartl, and J. G. Fujimoto, Opt. Lett. **28**, 2064–2066 (2003).
[32] B. Graf and S. A. Boppart, IEEE J. Sel. Top. Quantum Electron. in press (2012).
[33] Q. Wu, B. E. Applegate, and A. T. Yeh, Biomed. Opt. Express **2**, 1135–1146 (2011).
[34] J. Park, J. A. Jo, S. Shrestha, P. Pande, Q. Wan, and B. E. Applegate, Biomed. Opt. Express **1**, 186–200 (2010).
[35] E. B. van Munster and T. W. J. Gadella, Microscopy Techniques **95**, 143–175 (2005).
[36] H. G. Breunig, H. Studier, and K. Konig, Opt. Express **18**, 7857–7871 (2010).
[37] M. Peter and S. M. Ameer-Beg, Biol. Cell **96**, 231–236 (2004).
[38] M. C. Skala, K. M. Riching, A. Gendron-Fitzpatrick, J. Eickhoff, K. W. Eliceiri, J. G. White, and N. Ramanujam, Proc. Natl. Acad. Sci. U.S.A. **104**, 19494–19499 (2007).
[39] W. Y. Sanchez, T. W. Prow, W. H. Sanchez, J. E. Grice, and M. S. Roberts, J. Biomed. Opt. **15**, 046008 (2010).
[40] H. W. Wang, V. Gukassyan, C. T. Chen, Y. H. Wei, H. W. Guo, J. S. Yu, and F. J. Kao, J. Biomed. Opt. **13**, 054011 (2008).

[41] V. V. Ghukasyan and F. J. Kao, J. Phys. Chem. C **113**, 11532–11540 (2009).
[42] C. Vinegoni, T. Ralston, W. Tan, W. Luo, D. L. Marks, and S. A. Boppart, Appl. Phys. Lett. **88**, 053901 (2006).
[43] B. W. Graf, Z. Jiang, H. Tu, and S. A. Boppart, J. Biomed. Opt. **14**, 034019 (2009).
[44] B. W. Graf, S. G. Adie, and S. A. Boppart, Opt. Lett. **35**, 3120–3122 (2010).
[45] P. Stoller, B.-M. Kim, A. M. Rubenchik, K. M. Reiser, and L. B. D. Silva, J. Biomed. Opt. **7**, 205–214 (2002).
[46] H. D. Vishwasrao, A. A. Heikal, K. A. Kasischke, and W. W. Webb, J. Biol. Chem. **280**, 25119–25126 (2005).
[47] E. Houben, K. De Paepe, and V. Rogiers, Skin Pharm. Phys. **20**, 122–132 (2007).
[48] J. A. Izatt, M. R. Hee, G. M. Owen, E. A. Swanson, and J. G. Fujimoto, Opt. Lett. **19**, 590–592 (1994).
[49] B. H. Park, C. Saxer, S. M. Srinivas, J. S. Nelson, and J. F. de Boer, J. Biomed. Opt. **6**, 474–479 (2001).
[50] S. Sakai, M. Yamanari, Y. Lim, N. Nakagawa, and Y. Yasuno, Biomed. Opt. Express **2**, 2623–2631 (2011).
[51] H. J. Ko, W. Tan, R. Stack, and S. A. Boppart, Tissue Eng. **12**, 63–73 (2006).
[52] X. Liang and S. A. Boppart, IEEE Trans. Biomed. Eng. **57,** 953–959 (2010).
[53] B. F. Kennedy, X. Liang, S. G. Adie, D. K. Gerstmann, B. C. Quirk, S. A. Boppart, and D. D. Sampson, Opt. Express **19**, 6623–6634 (2011).
[54] R. John, R. Rezaeipoor, S. G. Adie, E. J. Chaney, A. L. Oldenburg, M. Marjanovic, J. P. Haldar, B. P. Sutton, and S. A. Boppart, Proc. Natl. Acad. Sci. U.S.A. **107**, 8085–8090 (2010).